

# Bayesian inversion of marine CSEM data from the Scarborough gas field using a transdimensional 2-D parametrization

Anandaroop Ray,<sup>1,\*</sup> Kerry Key,<sup>1</sup> Thomas Bodin,<sup>2</sup> David Myer<sup>3</sup> and Steven Constable<sup>1</sup>

<sup>1</sup>*Scripps Institution of Oceanography, La Jolla, CA 92037, USA. E-mail: a.ray@chevron.com*

<sup>2</sup>*Berkeley Seismological Laboratory, Earth and Planetary Sciences, University of California, Berkeley, CA 94720, USA*

<sup>3</sup>*BlueGreen Geophysics, Encinitas, CA 92023, USA*

Accepted 2014 September 17. Received 2014 August 16; in original form 2014 April 4

## SUMMARY

We apply a reversible-jump Markov chain Monte Carlo method to sample the Bayesian posterior model probability density function of 2-D seafloor resistivity as constrained by marine controlled source electromagnetic data. This density function of earth models conveys information on which parts of the model space are illuminated by the data. Whereas conventional gradient-based inversion approaches require subjective regularization choices to stabilize this highly non-linear and non-unique inverse problem and provide only a single solution with no model uncertainty information, the method we use entirely avoids model regularization. The result of our approach is an ensemble of models that can be visualized and queried to provide meaningful information about the sensitivity of the data to the subsurface, and the level of resolution of model parameters. We represent models in 2-D using a Voronoi cell parametrization. To make the 2-D problem practical, we use a source–receiver common midpoint approximation with 1-D forward modelling. Our algorithm is transdimensional and self-parametrizing where the number of resistivity cells within a 2-D depth section is variable, as are their positions and geometries. Two synthetic studies demonstrate the algorithm's use in the appraisal of a thin, segmented, resistive reservoir which makes for a challenging exploration target. As a demonstration example, we apply our method to survey data collected over the Scarborough gas field on the Northwest Australian shelf.

**Key words:** Inverse theory; Probability distributions; Non-linear electromagnetics; Marine electromagnetics; Australia.

## 1 INTRODUCTION

The marine controlled source electromagnetic (CSEM) method is an active source sounding method that has been in use for over three decades for the detection of geology with high resistivity contrasts (Young & Cox 1981; Chave & Cox 1982). Industry funded research and extensive commercialization of this technology over the last decade has led to CSEM being added to the standard suite of seismic methods in an exploration scenario (Ellingsrud *et al.* 2002; Constable 2010). Conductive media such as sea water or brine filled sediments have a characteristic electromagnetic scale length (skin depth)  $\delta = \sqrt{\frac{2}{\mu\omega\sigma}}$  that is dependent on both the medium conductivity  $\sigma$  and the frequency of propagation  $\omega$ , where  $\mu$  is the permeability of the medium. Owing to the fact that  $\delta$  is smaller in conductive media, marine geophysical EM methods almost always operate in the lower frequency quasi-static regime. This allows for deeper penetration of the CSEM fields into the Earth, but as a consequence it is

more a diffusive process than wave like (Loseth *et al.* 2006). To first order, it is this diffusive decay which helps characterize the conductivity of a given medium. For hydrocarbon bearing geology, it is the high resistivity of the hydrocarbon accumulation with respect to its surroundings that produces a signature quite different from what would have been observed in the absence of hydrocarbons (e.g. Constable 2006).

Given this diffusive nature, the stratigraphic resolution of CSEM is much lower than that of the seismic method. However, the value of CSEM lies in its sensitivity to resistivity, which may be indicative of hydrocarbon saturation, and not seismic impedance, which is more indicative of geological structure. Given that the seismic amplitude response saturates quickly with gas saturation in a formation, CSEM may be able to tell apart fizz gas from a commercially viable hydrocarbon resource. As a consequence of its diffusive nature, robust inferences made from a CSEM survey are necessarily from inversion of the data, and not merely from examination of the data itself (Weiss 2007). Typically, regularized and linearized gradient-based inversion methods have been used to arrive at models that minimize data misfit and are also 'optimal' in some user-defined sense. For

\* Now at: Chevron U.S.A. Inc.

instance, models can be pre-determinedly smooth or prejudiced to be close to a reference model. By means of regularization, highly oscillatory features in the model that are thought to be outside the resolution of CSEM are suppressed (e.g. Constable *et al.* 1987; MacGregor & Sinha 2000; Newman & Alumbaugh 2000; Abubakar *et al.* 2008; Key 2009; Mitter & Gabrielsen 2013; Sasaki 2013). Though gradient-based inversion methods are highly efficient and well understood, they provide only a single smooth model as a result, or a suite of smooth models. These models provide a limited insight into the various classes of models that are compatible with the observed data given the noise. Furthermore, a clear understanding of the resolvability of subsurface resistivity and non-uniqueness of the final solution does not emerge from a linearized treatment of the non-linear CSEM problem.

To quantify the uncertainty inherent in the inversion of CSEM data, one can utilize a Bayesian framework where information is expressed as probability density functions or PDFs. Since Bayesian probability (Bayes & Price 1763) is a measure of information and since it is the aim of geophysical inversion to provide information about the Earth's subsurface, it is natural to postulate geophysical inverse problems in a Bayesian framework (Tarantola & Valette 1982; Mosegaard & Tarantola 1995; Scales & Sneider 1997). In such a framework, model parameters are treated as random variables, and their fit to the observed data given the observed statistical noise allows one to formulate a model likelihood. To make the connection with deterministic inversion methods, to first order, models with low misfit possess a higher likelihood. After incorporating prior knowledge of the models that is independent of the data, the product of the prior model probability and the likelihood is known as the posterior model probability. This posterior PDF describes the full solution to the inverse problem—it represents the probability of the model, given the observed data. Those parts of the model space that are more frequently required by the data than other parts manifest with greater posterior probability, and hence are more certain to be properties of the Earth (Backus 1988).

Our study is not the first to apply Bayesian methods for inversion of marine CSEM data. One of the earliest applications focused on joint inversion of CSEM and seismic data in order to improve estimates of reservoir properties (Hou *et al.* 2006; Chen *et al.* 2007). Gunning *et al.* (2010) use a hierarchical Bayesianized bootstrap scheme for CSEM inversion. Trainor-Guitton & Hoversten (2011) use a sampling scheme which involves both the Metropolis–Hastings algorithm (Hastings 1970) and slice sampling (Neal 2003) in order to improve convergence upon the PDF of solution models. Buland & Kolbjornsen (2012) apply the Metropolis–Hastings algorithm to invert marine CSEM data together with magnetotelluric (MT) data in order to constrain the range of likely resistivities as a function of depth. In all these studies, with the exception of Gunning *et al.* (2010) who use a maximum *a posteriori* estimate-based layer splitting approach, the parametrization is fixed at the outset by the user. However, fixing a particular model parametrization (e.g. fixing the number of layers or cells) for the inversion is known to produce posterior PDFs, ‘only’ for the given parametrization (Dettmer *et al.* 2010). This is where the ‘transdimensional’ or ‘reversible jump’ (Green 1995) Markov chain Monte Carlo (RJ-MCMC) differs from traditional MCMC methods (e.g. Gilks *et al.* 1996), in sampling from a posterior PDF where the number of unknowns (i.e. the parametrization) is also treated as part of the inverse problem. In other words, the parametrization is also inferred from the observed data. A review of applications which use transdimensional MCMC can be found in Sisson (2005). Such algorithms have a ‘parsimony’ property (Malinverno 2002), which

refers to the fact that Bayes’ theorem deems models that explain the data with simpler parametrizations more probable. MacKay (2003) discusses this aspect of Bayes’ theorem in some detail. Malinverno (2002) was the first to use this method in a geophysical application for DC resistivity inversion. Sambridge *et al.* (2006) further discuss this method in the context of evidence-based model selection (Bernardo & Smith 1994; Denison 2002). Bodin & Sambridge (2009) use transdimensional MCMC for solving the seismic surface wave tomography problem. Agostinetti & Malinverno (2010) have used this method for receiver function inversion, as have Bodin *et al.* (2012). Recent applications of the transdimensional method to solve geophysical EM methods can be found in Minsley (2011) and Brodie & Sambridge (2012), who apply it the airborne EM problem, and in Ray & Key (2012), who tackle the marine CSEM problem. An introduction to geophysical transdimensional Bayesian inversion can be found in Sambridge *et al.* (2013).

For probabilistic inversion, the final solution is a large ensemble of models which are statistically distributed according to a posterior model PDF. As this involves a direct parameter search, hundreds of thousands of models must be evaluated and sampled before convergence to the desired posterior model PDF. This computational expense has largely limited the application of Bayesian methods for highly non-linear problems to those with a computationally efficient 1-D model parametrization. Notable exceptions can be found in the work of Chen *et al.* (2012) and Rosas-Carbajal *et al.* (2013). However, though both of these works invert 2-D MT and plane wave electrical resistivity tomography (ERT) data, respectively, they use a fixed number of parameters. JafarGandomi & Binley (2013) use a transdimensional approach to invert multiple data sets within a 2-D depth section, but only the vertical parametrization is transdimensional while the lateral parametrization is fixed. Fully two-dimensionally parametrized, transdimensional inversions have been carried out only within the last 5 yr. For example, Bodin & Sambridge (2009) perform seismic surface wave tomography using Voronoi cells in a transdimensional formulation. Luo (2010) finds the shapes of bodies which cause a gravity anomaly (given a fixed density contrast). Young *et al.* (2013a,b) use transdimensional inversion for *P* wave tomography and seismic ambient noise inversion. Dettmer & Dosso (2013) use this approach for geoacoustic inversion. To the best of our knowledge, this work is the first transdimensional Bayesian inversion that uses a true 2-D model parametrization with Voronoi cells for the inversion of geophysical EM data.

After validating our methodology using synthetic examples, we invert CSEM data from over the Scarborough gas field on the Exmouth Plateau, off the North West Australian shelf (Myer *et al.* 2010, 2012).

## 2 THEORY

### 2.1 Bayesian inversion with the RJ-MCMC algorithm

Bayesian information is contained in PDFs represented by  $p(\cdot)$ . Using Bayes’ theorem, we write

$$p(\mathbf{m}|\mathbf{d}) = \frac{p(\mathbf{d}|\mathbf{m}) \cdot p(\mathbf{m})}{p(\mathbf{d})}. \quad (1)$$

For Bayesian geophysical inversion, the observed data vector  $\mathbf{d}$  is a constant. All PDFs with a model dependence are functions of the random variable  $\mathbf{m}$ . The term  $p(\mathbf{d}|\mathbf{m})$  can then be interpreted as the model likelihood, the functional form of which depends on the statistics of the noise distribution, and the value of which depends

on the model  $\mathbf{m}$  being sampled and its fit to observed data. For Gaussian noise, the model likelihood is given as

$$p(\mathbf{d}|\mathbf{m}) \propto \exp\left(-\frac{[\mathbf{d} - f(\mathbf{m})]^T \mathbf{C}_d^{-1} [\mathbf{d} - f(\mathbf{m})]}{2}\right). \quad (2)$$

Here,  $f(\mathbf{m})$  corresponds to the modelled data and  $\mathbf{C}_d$  is the covariance matrix of the residual data errors including theory error and  $[\mathbf{d} - f(\mathbf{m})]^T \mathbf{C}_d^{-1} [\mathbf{d} - f(\mathbf{m})]$  is the  $\chi^2$  misfit for the evaluated model  $\mathbf{m}$ . Care must be taken to ensure that for complex observed data (such as frequency domain data) where the total variance equals twice that of the real or imaginary parts, the factor of 2 should be removed from eq. (2) and that the vector transpose should be Hermitian (see the chapter on circularly symmetric complex random variables in Vaidyanathan *et al.* 2010).

For marine CSEM, the Fourier coefficients at the frequencies of interest are stacked over non-overlapping time windows to produce Gaussian data errors through central limiting. This enables us to use a Gaussian likelihood function. However, uncertainty in the transmitter position, theory error and insufficient model parametrization among various other factors can lead to correlated error in the observed data. Since correlated error violates the assumption of independent data noise it can manifest in spurious structure in inverted models. Hierarchical Bayesian approaches to estimating  $\mathbf{C}_d$  where  $\mathbf{C}_d$  is itself ‘sampled’ can be used (e.g. Gelman *et al.* 1995; Carlin & Louis 2000; Malinverno & Briggs 2004; Bodin *et al.* 2012; Dettmer *et al.* 2012; Ray *et al.* 2013b; Steininger *et al.* 2013). Such an approach is not the focus of this work though it is an active area of research.

The prior model PDF  $p(\mathbf{m})$  represents our state of knowledge ‘independent’ of the survey data. The evidence term  $p(\mathbf{d})$  corresponds to a constant PDF normalizing factor equal to the integral over all models of the numerator in eq. (1). The evidence allows us to perform ‘model selection’ (Bernardo & Smith 1994; Denison 2002; MacKay 2003) or the process of deciding which model parametrization is more probable than the other—for example, should we use two cells as opposed to three to represent the subsurface? However, evidence is very challenging to compute as it requires evaluation of a multidimensional integral over different models, evaluated for different model parametrizations. Another means of performing model selection is to use a hierarchical Bayesian scheme to estimate the posterior PDF over multiple models of interest, that is, estimate a transdimensional posterior  $p(\mathbf{m}|\mathbf{d})$  where all models of interest are considered simultaneously according to their support by the data (Sambridge *et al.* 2006; Dettmer *et al.* 2010). This is the RJ-MCMC approach that we have used in this paper, which is different from the usual MCMC approach in the following manner: Treating the evidence as a proportionality constant, it follows from eq. (1) that

$$p(\mathbf{m}|\mathbf{d}) \propto p(\mathbf{d}|\mathbf{m}) \times p(\mathbf{m}). \quad (3)$$

In the transdimensional method, for a given model  $\mathbf{m}$ , we split the prior PDF  $p(\mathbf{m})$  into two parts. One part contains information about the number of cells  $k$  in the model,  $p(k)$ . The other part  $p(\mathbf{m}_k|k)$  contains information about their physical properties such as the locations of the cells and what the resistivities of these cells are, given the number of cells  $k$ . Thus, it follows from eq. (3) that

$$p(\mathbf{m}|\mathbf{d}) \propto p(\mathbf{d}|\mathbf{m}) \times p(\mathbf{m}_k|k) \times p(k). \quad (4)$$

This formulation allows the parametrization to be an unknown in the problem. Our task is to evaluate uncertainty in the models inverted from the observed data. To this end, we must arrive at the posterior PDF of models, most of which fit the data well, by evaluating

their misfit and sampling models according to eq. (4). However, it is nearly impossible to exhaustively sample the model space for more than a few parameters owing to the ‘curse of dimensionality’, hence we resort to probing this highly non-linear PDF using various MCMC methods (e.g. Gilks *et al.* 1996; Liang *et al.* 2011) and focus on the RJ-MCMC or transdimensional method.

## 2.2 Parametrization with Voronoi cells

Voronoi cells are an efficient topology for parametrizing a 2-D space (Voronoi 1908). They can represent various complicated geometries, and their tessellations are simple to compute (Okabe *et al.* 2009). We can specify a set of points (Voronoi nodes) in a bounded plane, and for each node there will be a corresponding region consisting of all points closer to that node than to any other node. These regions are called Voronoi cells. For geophysical problems, this parametrization presents itself as a convenient means to assign Voronoi cells with properties such as velocity (Bodin & Sambridge 2009; Dettmer & Dosso 2013) or as we propose to do in this work, resistivity. Only the Voronoi nodes and their locations need to be kept track of. This is shown in Fig. 1, where a tabular body of resistivity 100 ohm-m in a 1 ohm-m background has been approximated almost perfectly by a sparse Voronoi representation with five cells. It should be noted that this Voronoi diagram is not the solution to a geophysical inverse problem but merely an example illustrating its use in simple representations of common shapes. Details on how Voronoi cells are used to construct a 2-D spatial posterior PDF are given in Section 3.2.

## 2.3 Forward modelling and parametrization

For a given transmitter–receiver (Tx–Rx) separation, we use the approximation that observed data are primarily sensitive to the vertical profile of seafloor resistivity at the Tx–Rx midpoint (Mittet *et al.* 2008; Gunning *et al.* 2010; Silva Crepaldi *et al.* 2011). This is similar to a common midpoint formulation (CMP) used in

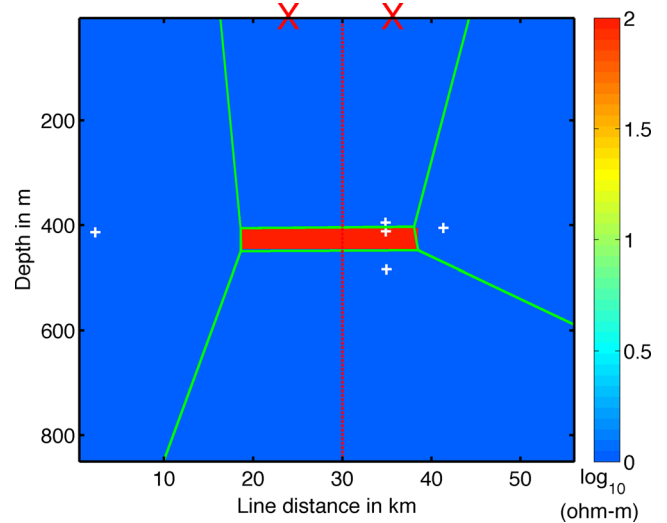


**Figure 1.** Five Voronoi cells being used to approximate a rectangular reservoir in a uniform background. The nodes are shown with white plus signs. The cells are entirely defined by their node positions, as the edges (green lines) run through the perpendicular bisectors between neighbouring nodes. A profile through the reservoir (dashed red) is located at a source–receiver midpoint with source and receiver locations each marked by an X.

reflection seismology. This 1-D approximation is numerically far less expensive than modelling the full 2-D problem. A 2-D model forward evaluation, depending on the geological complexity of the model, the number of frequencies and parallel cores used, may take from a few seconds to minutes (Key & Ovall 2011). However, 1-D evaluations across all CMPs for a 50-km long 2-D line takes little more than half a second on average. We use 2-D Voronoi cells to parametrize the vertical cross-section of the Earth in a profile along the survey line (e.g. Dettmer & Dosso 2013). For each CMP, a vertical profile is extracted through this Voronoi cell parametrization as shown in Fig. 1. The response due to this 1-D profile, at the given Tx–Rx offset and data frequencies is calculated using Dipole1D (Key 2009). Since we use Voronoi cells to parametrize a 2-D depth section, a vertical profile can be extracted anywhere within this section. This ensures that there is no restriction on locations of sources or receivers along a linear profile. Care must be taken to ensure that the CMP approximation is only applied till a maximum offset length, which is target geology dependent. In general, longer offset data display 2-D or 3-D behaviour that should not be used for inversion with a CMP approximation.

## 2.4 Transdimensional Bayesian inversion

In the simplest terms, the objective of transdimensional Bayesian inversion is to sample the model PDF given by (4). This is achieved with the RJ algorithm by drawing candidate models from a proposal PDF. These models are then examined to see if they fall within geophysically sensible uniform bounds of resistivity and depth. If a proposed model falls outside the prior PDF, it is rejected and the Markov chain retains the previous model as the next model. If a proposed model is within the prior bounds, an acceptance probability is calculated using a ratio of the proposal probability, the prior probability and the likelihood of the candidate model with respect to the previous model. The proposed model is either accepted with the calculated probability and it becomes the next model in the chain, or it is rejected and the previous model is retained as the next in the chain. Complete details of this process are given in the Appendix for the interested reader. As the algorithm proceeds, hundreds of thousands of models are sampled, with a data-driven addition or deletion of Voronoi nodes ('birth/death' in RJ-MCMC parlance), such that a chain of models, most of which fit the data well within the noise, are retained at the end. To ensure thorough sampling of this multi-dimensional parameter space, various independent Markov chains with different starting models are run in parallel and finally concatenated into a model ensemble that is representative of the sought after posterior model PDF (4).

## 3 2-D SEGMENTED RESERVOIR EXAMPLE

In order to validate our methodology, we created a 60-km-long synthetic model, with a 1-km-deep sea water layer and a 30-km-long, 30-m-thick segmented reservoir buried at 1 km below the seafloor (Fig. 2). The resistivity segments for the reservoir are 30, 10 and 5 ohm-m, tapering away from the centre. The background resistivity is 1 ohm-m. Given that the reservoir is thin and that the resistivity contrasts are not very high, this presents a challenging exploration target. This geometry is motivated by the size and shape of the Scarborough reservoir in the NW Australian shelf (Myer *et al.* 2010), which we consider later in this work. Synthetic data were forward calculated using the 2.5-D adaptive finite element

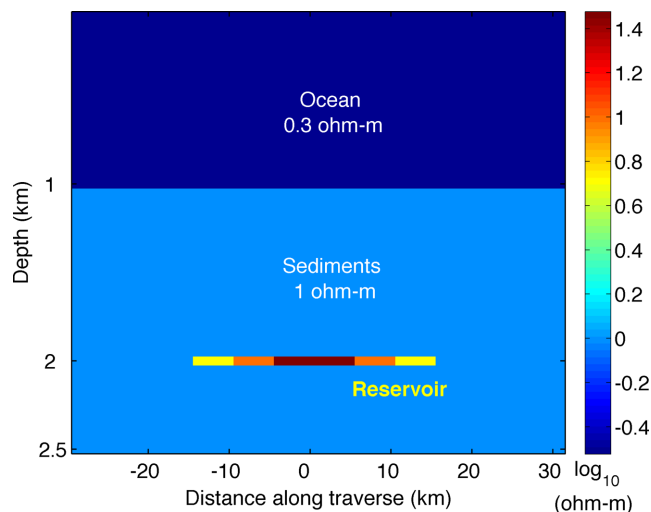


**Figure 2.** A 30-km long, 30-m thin synthetic segmented resistor model representative of the Scarborough reservoir.

code of Key & Ovall (2011). Gaussian noise at 5 per cent of the signal amplitude was added to the data at four different frequencies of 0.1, 0.3, 0.7 and 1.1 Hz. Receivers recording the inline electric field were spaced every 500 m along the line.

## 3.1 1-D modelling and inversion through the central segment

Before embarking on the inversion of 2-D data, we examine a 1-D Bayesian inversion of 1-D responses from the central part of the segmented reservoir model to highlight some salient features of Bayesian inversion. We use the 1-D CSEM code and inversion algorithm described in Ray & Key (2012). 96 independent, parallel MCMC chains with 500 000 models in each chain were sampled to form a posterior model PDF. This inversion required 4 hr on 96 CPU cores (dual socket @2.6 GHz). 50 random models from the sampled posterior, along with their data fits in phase and amplitude are shown in Fig. 3. The true model is shown in red in the leftmost panel.

To visualize the full posterior PDF, we separately bin the resistivities and interfaces at 10-m depth intervals. The resulting marginal

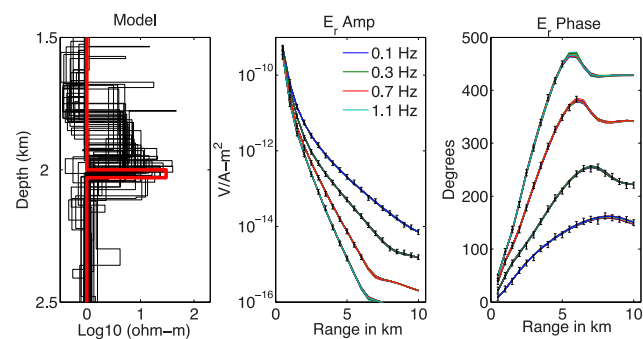


**Figure 3.** Inversion of noisy, synthetic radial electric field data  $E_r$  calculated from the 1-D reservoir corresponding to the centre of the 2-D segmented reservoir model. The true 1-D model is shown in red in the left-hand panel, with 50 randomly selected models from the posterior PDF  $p(\mathbf{m}|\mathbf{d})$  shown in black. The responses due to these models, along with the observed data are shown as  $E$  field amplitude (centre panel) and phase (right-hand panel) plots with range.

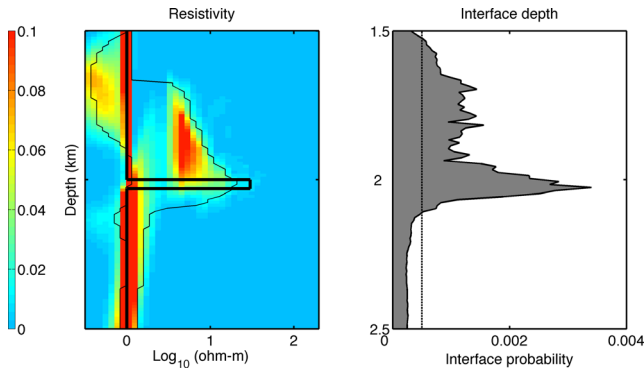


**Figure 4.** Marginal PDFs on resistivity (left-hand panel) and interface depth (right-hand panel) from the 1-D synthetic data inversion with true model corresponding to the 1-D segment through the centre of the 2-D synthetic model. The true model is shown with a thick black line in the left-hand panel. The 5 and 95 per cent quantiles on resistivity with depth are shown as thin black lines on the left-hand panel. Hotter colours are more probable.

densities on resistivity and interfaces at depth are shown in Fig. 4. The 5 and 95 per cent quantiles on resistivity with depth are shown in the left-hand panel as thin black lines. Hotter colours correspond to higher probabilities in the left-hand panel. It can be seen that the true reservoir resistivity is not the most probable, that it is even outside the 95 per cent quantile, but we do see a clear trend in sampled resistivities increasing with depth and then returning to a background value. The fact that the true values are not the most probable, though not intuitive, is not new as has been shown by Ray *et al.* (2013a). This should serve as a note of caution to prevent researchers from picking the mode of any posterior model PDF as the ‘truth’. This seems to be a statement of the fact that there are many more different ways to fit the data within the noise, than with the very delta function like true model. In fact, one can clearly see the well-known CSEM trade-off between thicker, less resistive layers and thinner, more resistive layers (e.g. Constable & Weiss 2006). It is worthwhile to point out that such trade-offs cannot be quantified by any single result from a conventional gradient-based deterministic inversion scheme. The interface probabilities in the right-hand panel do show a pronounced peak in the probability of interfaces at the right depths. For a thin reservoir, this seems to imply good sensitivity to the bottom.

### 3.2 Inversion of 2-D data with the CMP approach

In this section, we present the inversion of the noisy synthetic 2-D data from the segmented reservoir model using the transdimensional Voronoi parametrization and the CMP approach. During the inversion, we calculate the forward responses for 1-D profiles through the Voronoi tessellation at every CMP location. 96 independent, parallel RJ-MCMC chains were run on 96 CPU cores (dual socket @2.6 GHz), out of which 92 chains converged to acceptable rms (root mean square) values. We would like to point out here that not all Markov chains are able to escape local probability maxima within the given run time. Each chain sampled  $10^6$  models but the first half of the chain is thrown away to achieve ‘burn-in’ to rms values between 1.2 and 1.3. Given that the model physics is approximate and parametrization not the same as was used to create the forward model, we do not expect the mean rms misfit of the sampled models to be exactly 1.0. Posterior PDFs on all parameters of interest were analysed for the first half and then

the second half of the post burn-in samples. As the two sets of PDFs were found to be similar, the ensemble was deemed to have achieved convergence. More details on convergence are given in the Appendix. Uniform prior bounds require models to possess resistivities between 0.3 and 200 ohm-m, and from 10 to 150 nodes placed between 1 and 3-km depth anywhere within the 60-km long 2-D line.

To illustrate the process of forming the posterior model ensemble, one MCMC chain is shown in Fig. 5. All converged chains can be concatenated to form an ensemble of models like the one shown in the figure. One slice shows an arbitrary 2-D model parametrized by Voronoi cells. The other perpendicular slice, near the beginning of the line, shows resistivities in vertical section across all sampled models. A histogram of resistivities with depth can be made from the vertical section to produce a display akin to the left-hand panel in Fig. 4. Furthermore, such histograms can be made from all vertical slices along the 2-D line to form a probability cube, with axes being resistivity, line distance and depth, as shown in Fig. 6. A vertical

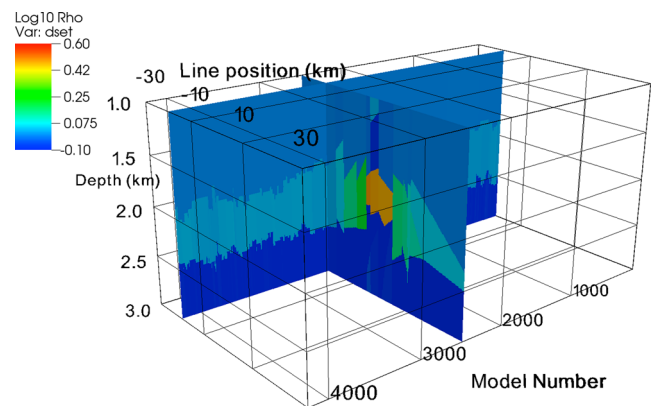


**Figure 5.** Example MCMC chain from the segmented reservoir inversion. Here we show both a particular Voronoi cell model #2500 and a vertical slice across all models at  $-20$  km along the line. Colours correspond to  $\log_{10}$  of resistivity.

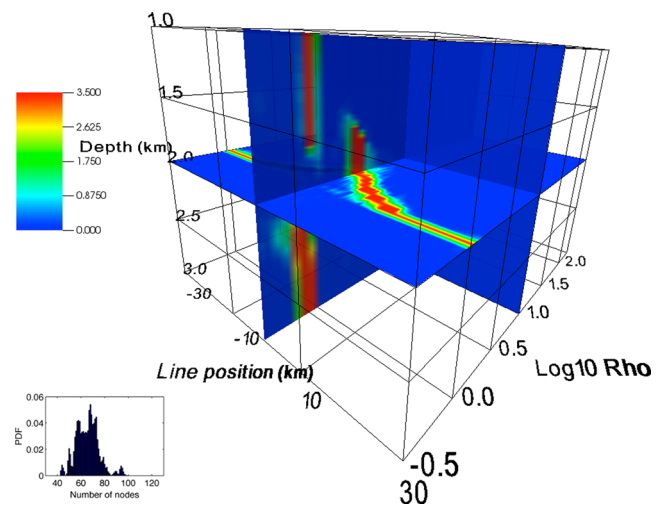


**Figure 6.** Slices through a probability cube from the segmented reservoir inversion, with axes representing  $\log_{10}$  resistivity, position along the 2-D line and depth. The probability cube is made from histograms of all MCMC chains such as the one shown in Fig. 5. Hotter colours correspond to higher probabilities. The inset box shows the PDF on the number of Voronoi nodes required to form the probability cube.

slice of the probability cube through the centre of the 2-D line (the central segment of the reservoir) shows that there is a clear rise in the resistivity of the subsurface with depth and then a return to the background. A horizontal slice at 2000-m depth shows a clear increase in resistivities from a 1 ohm-m background as we move along the survey line, increasing in steps and symmetrically decreasing as we would expect for the segmented reservoir. Also shown in this figure is the PDF on the number of Voronoi cells (nodes) required to form the displayed probability cube. Note how the algorithm does not cluster around the maximum or minimum possible number of nodes (10 and 150) required to fit the observed data.

Based on the experience of our 1-D modelling study showing the posterior trade-off between resistivity and reservoir thickness, we would not expect the most probable resistivities sampled to be the true values, and this is indeed the case. The maximum sampled resistivity (Fig. 6) is around 10 ohm-m at the reservoir depth in the central segment, which is quite distant from the true value of 30 ohm-m. However, the probability of the integrated resistivity thickness product  $\tau = \int \rho(z) dz$  between 1500 and 2500-m depth, containing the reservoir interval, yields some valuable insights, as can be seen in Fig. 7. True values are shown with black lines, and the background and segmented reservoir  $\tau$  values are clearly visible as falling within the probable parts of the marginal PDF. Previous studies have shown that  $\tau$  seems to be a more robust indicator of reservoir presence than resistivity alone (Constable & Weiss 2006; Myer *et al.* 2012; Connell & Key 2013). The posterior probabilities on this quantity bolster this idea. For instance, even if we were to pick the mode of this PDF in Fig. 7 near the centre of the line, though 1700 ohm-m<sup>2</sup> is less than the true value of 1870 ohm-m<sup>2</sup>, it would not lead to a bad estimate of the reservoir resistivity. Assuming a 30-m-thick resistive layer and a 1 ohm-m background, this  $\tau$  value is consistent with a 24 ohm-m reservoir resistivity. Often such information on thickness is available from an external source such as seismic imaging. Conversely, if the true resistivity of 30 ohm-m was known, for example from well-logs, we could then estimate a probable thickness of 24 m which is not too far from the true value of 30 m.

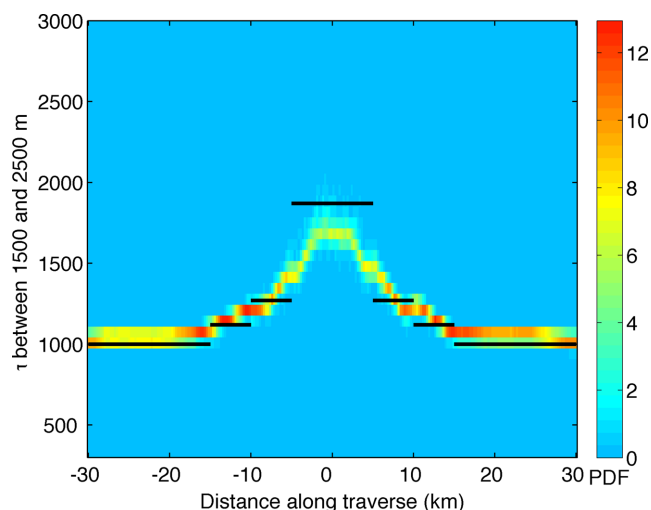


**Figure 7.** Probability of the integrated resistivity thickness product  $\tau$  between 1500 and 2500-m depth from the segmented reservoir inversion. Black lines show the true values corresponding to the background and reservoir segments. Hotter colours are more probable.

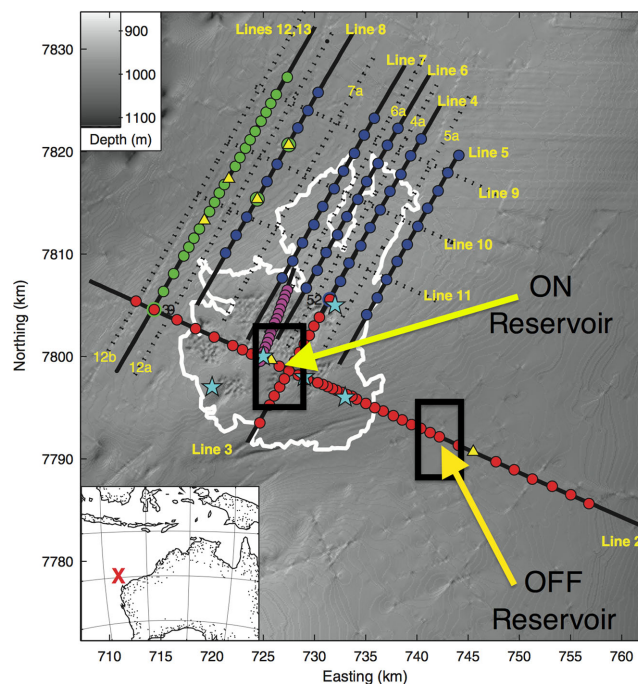


**Figure 8.** A map of the Scarborough reservoir outline (white) overlaid on the bathymetry. Instruments were deployed at points marked by filled circles in four phases coloured red, blue, green and magenta. In this work, we have focused on the flagship Line 2 towards the south. Modified from Myer *et al.* (2012).

## 4 REAL DATA: SCARBOROUGH GAS FIELD ON THE EXMOUTH PLATEAU, NW AUSTRALIAN SHELF

### 4.1 Regional geology and reservoir setting

In this section, we apply our methodology to data from the Scarborough gas field, which lies inside the Exmouth Plateau. The plateau (Fig. 8) is a passive margin between continental and oceanic crust which remains after the break-up of Australia and India, and is surrounded on three sides by oceanic crust at abyssal depths. The plateau, which is  $\sim 400$  km  $\times$  600 km, is bounded to the northeast and southwest by transform faults. The transition between continental and oceanic crust to the northwest is thought to be bounded by a subhorizontal detachment fault that undercuts the plateau at about 10-km depth, dipping towards the Australian continent (Driscoll & Karner 1998). Since the Mesozoic era, the plateau has undergone a complex sequence of fracture, extension, uplift, truncation and subsidence. The result is that the plateau is covered by a number of mostly horizontal sedimentary layers of resistivities varying between 1 and 10 ohm-m (Myer *et al.* 2012).

Five exploration wells have been drilled in the Scarborough gas field and their data, combined with 3-D seismic coverage, were used to define the areal extent and section profile of the reservoir. The white contour in Fig. 8 is the 50 per cent gas saturation line. The reservoir itself (Fig. 9) is a 20–30 m layer residing between 1900 and 2000 m below sea level (mbsl) in about 900–950 m of water. It has a moderate resistivity of 25 ohm-m and is overlain by several thin layers of lower gas saturation with resistivities of 5–10 ohm-m.

### 4.2 Scripps 2009 survey and previous work in 1-D

CSEM and MT data were collected during a month long research cruise using the Scripps Institution of Oceanography's R/V Roger

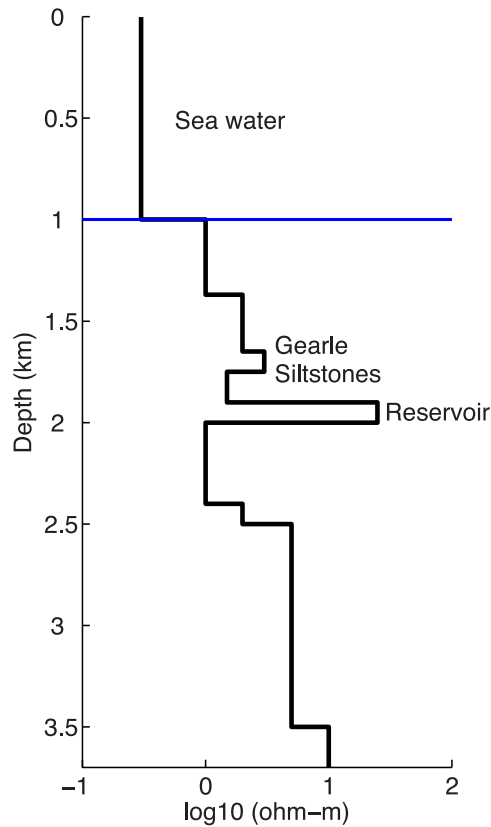


**Figure 9.** Simplified cross-section of Scarborough reservoir electrical resistivity structure, reproduced from Myer *et al.* (2012)

Revelle (Fig. 8). Details of the CSEM acquisition and MT mapping of a deep subhorizontal conductive layer can be found in Myer *et al.* (2011, 2012) and Myer *et al.* (2013), respectively. In this work, we have concentrated our efforts on inverting the inline electric field CSEM data at frequencies of 0.25, 0.75, 1.75 and 3.25 Hz acquired over the  $\sim 50$ -km-long Line 2 to the south.

The reservoir is not a large CSEM target, as the  $\tau$  value is only  $\sim 900$  ohm-m<sup>2</sup> above the background levels of  $\sim 200$  ohm-m<sup>2</sup> for the reservoir section. This difference is much less than typical transverse resistances of  $10^4$  considered in many past marine CSEM model studies (Constable & Weiss 2006; Myer *et al.* 2012). Furthermore, there is a confounding overlying layer in the form of the resistive Gearle siltstones between 1650 and 1750 mbsl (Veevers & Johnstone 1974), which may make it difficult to tease apart the reservoir layer and the Gearle siltstones without *a priori* information, as reported by Myer *et al.* (2012) and illustrated in Fig. 10. Without introducing cuts in the inversion to separately delineate the siltstones and the reservoir, the Occam1DCSEM inversion (thick black line) was unable to distinguish these two layers from a single layer of moderately increased resistivity near reservoir depth. For 1-D comparison, we performed purely 1-D Bayesian inversions using the methodology of Ray & Key (2012) at both the on and off reservoir sites (Fig. 10). These inversions suggest that the posterior PDF of resistivities at reservoir depth on reservoir (bottom, left-hand panel) is more resistive than the PDF at the same depth off-reservoir (top, left-hand panel). Note that the 1-D RJ-MCMC Bayesian inversions did not utilize any prejudice models or roughness penalty cuts.

The separate transdimensional Bayesian results shown in Fig. 10 do indeed indicate that it is more probable to have a resistive

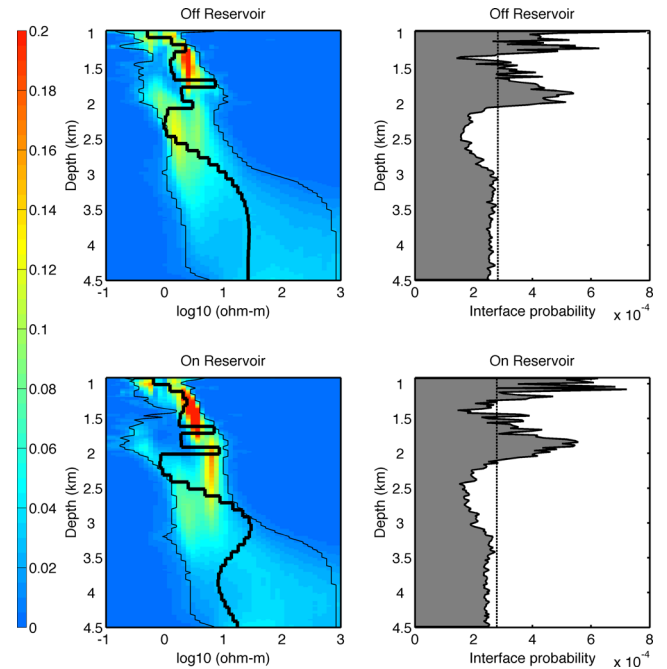


**Figure 10.** 1-D Occam's inversion results (thick black line) from Myer *et al.* (2012) with roughness penalty cuts at the reservoir and Gearle siltstone sections at sites off reservoir (top) and directly on reservoir (bottom) overlain on purely 1-D Bayesian inversion probabilities for resistivity with depth using the same data. The 5 and 95 percent quantiles on resistivity with depth are shown as thin black lines on the left-hand panels. The 1-D Bayesian inversions followed the methodology of Ray & Key (2012) and were performed separately.

reservoir at the on reservoir site than at the off reservoir site. However, these results follow from a 1-D parametrization, and PDFs of resistivity with depth at each site are independent of each other. Posterior inference on resistivities between these two sites can be performed using sequential Bayesian techniques (Yardim & Gerstoft 2012) but require the careful use of bridging distributions to evaluate 1-D resistivity posterior PDFs at adjacent sites (Dettmer *et al.* 2011). These considerations motivate the next part of this section on inverting the Scarborough CSEM data along Line 2 using a fully 2-D model parametrization and the RJ-MCMC method.

### 4.3 Results from 2-D parametrized transdimensional inversion using the CMP approach

An inversion with 160 independent parallel chains on 160 CPU cores (dual socket @2.6 GHz) was run on CSEM data acquired along Line 2. Four frequencies at 0.25, 0.75, 1.75 and 3.25 Hz were used, but Rx–Tx offsets were limited to 4 km for the observed data to be compatible with the 1-D forward model physics. Given that variations in bathymetry along the line are minimal (see Fig. 8), the 2-D models used a flat seafloor. The true Rx–Tx elevation and relative sea water conductivity stratification was maintained. Each chain sampled  $2 \times 10^6$  models, with the first half of the chain being thrown away to achieve sampled rms values between 1.28 and 2.08, with a total of 90 chains converging to acceptable values. The total run time was 192 hr. As with the synthetic example, posterior PDFs on all parameters of interest were analysed for the first half and then the second half of the post burn-in samples. As the two sets of PDFs were found to be similar, the ensemble was deemed to have

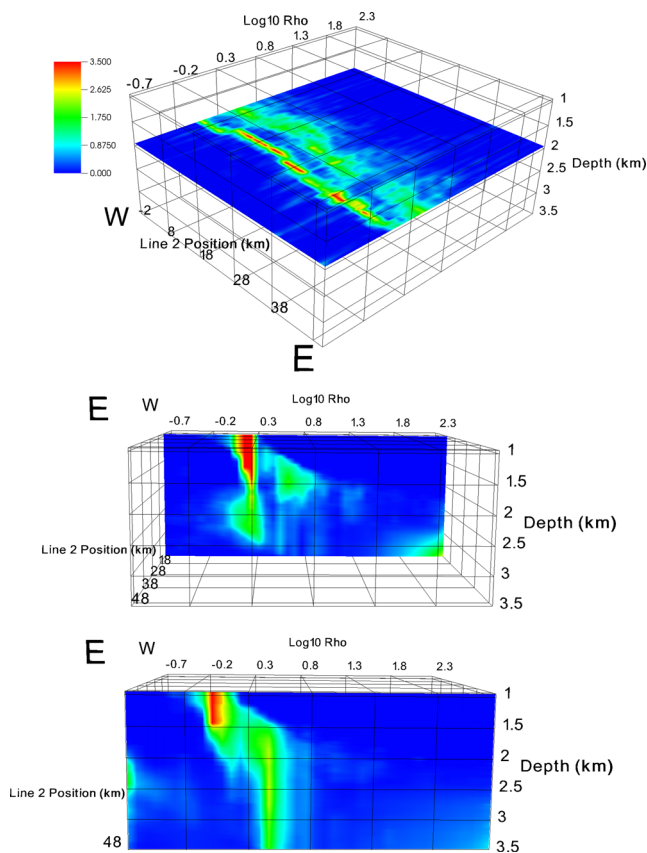


**Figure 11.** Top panel: A slice through the probability cube for the Scarborough data inversion at 1950-m depth. Hotter colours are more probable. Note the probability of increasing resistivity between 6 and 24 km along Line 2, indicative of reservoir. Middle panel: A slice through 11 km along the line (on reservoir), within the known reservoir outline shown head on. The probability of a 10 ohm-m resistive anomaly is seen clearly at 2000-m depth. Bottom panel: A slice through 50 km along the line (off reservoir area), 25 km east and outside of the known reservoir outline. The probability of a resistive anomaly at 2000-m depth has now all but disappeared.

achieved convergence. Uniform prior bounds require that models possess resistivities between 0.2 and 200 ohm-m, and from 20 to 400 nodes placed between 940.6 and 3500 m depth anywhere within the 50-km long 2-D line.

A probability cube with axes representing  $\log_{10}$  resistivity, Line 2 distance and depth was formed as is shown in Fig. 11. The top figure shows a horizontal slice at 1950 m depth (reservoir level). The background resistivity is well sampled in this slice, at around 1 ohm-m. The Gearle is also visible everywhere at 3.2 ohm-m in this horizontal slice (though it should be shallower, between 1650 and 1750 mbsl and not visible in the 1950 m slice). Most interestingly, between 6 and 24 km along Line 2, where the gas saturation was deemed to be greater than 50 per cent from seismic and petrophysical analyses, there is a gradual increase in resistivities such that they lie largely between 6.3 and 15.8 ohm-m. Given that we have not regularized or guided our inversion in any manner besides use very broad uniform parameters to sample within, this is a clear indication of a more resistive body in that section of line at  $\sim 1950$ -m depth. The middle figure shows a vertical section through 11 km position along the line, which lies in the middle of the reservoir outline on Fig. 8 (on reservoir). There is a clear increase in resistivity at 2-km depth to values of 10 ohm-m and

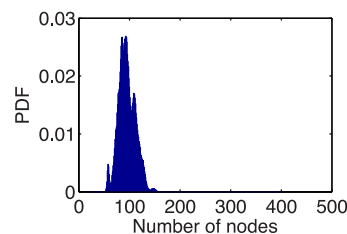


**Figure 12.** PDF on the number of Voronoi nodes required by the transdimensional inversion to fit the Scarborough CSEM data.

above, with a return to background values at deeper depths, with suggestions of a very resistive basement at 3-km depth. The bottom figure shows a vertical section through 50 km along Line 2, at the extreme east end of the line, 25 km outside the reservoir outline (off reservoir area). If we follow the PDF of resistivities along the line at 2-km depth from the middle figure to the bottom figure, the bulk of the models in the PDFs of resistivity at 2-km depth change from values above 10 ohm-m down to values close to 3.16 ohm-m. Thus, looking at all three parts of Fig. 11, we are able to infer that there is indeed a resistor at 1950–2000 m depth, the lateral extents of which are limited roughly between 6 and 24 km position along the line. We emphasize here that looking at the spatial changes in the PDFs of resistivity—as made possible by a Bayesian inversion, is a more robust method of interpreting geology, than looking at the changes in one single, inverted model from a regularized inversion method. The PDF on the number of Voronoi nodes required by the transdimensional inversion is shown in Fig. 12. Again, this PDF does not cluster either around the maximum or minimum possible number of nodes (20 and 400) and shows that the data require 50–150 nodes to be fit.

At this juncture, it is important to keep in mind that posterior data residuals could indeed be correlated to some degree—violating the assumption of spatially independent noise. As mentioned in the introduction, this could be due to a number of reasons, chiefly the acquisition systematics and the 1-D CMP approximation. This could lead to an incorrect estimation of the posterior PDF. However, previous work in 1-D has shown that even when the correlations are dealt with using an iterative hierarchical Bayesian scheme to sample the residual data error including the off-diagonal terms in  $C_d$ , the probability of a resistive interface at reservoir depth does not disappear (Ray *et al.* 2013b). Of course, to be completely rigorous, one should not only model the residual correlations but use 2.5-D or 3-D forward modelling codes, which we hope we will be able to do in future.

The probability of  $\tau$  between 1500 and 2500 m depth, illustrated in Fig. 13 (top panel), shows three modes corresponding to the background (1000–2000 ohm-m<sup>2</sup>), Gearle (2500–3000 ohm-m<sup>2</sup>) and the basement ( $> 10^4$  ohm-m<sup>2</sup>) resistivities. In addition, there is a clear departure from the Gearle resistivities in the same lateral section of line as the reservoir is known to be in. This is highlighted by the boxed area of Fig. 13 (top panel) and in the close view given in Fig. 13 (bottom panel). Furthermore, this anomaly is  $\sim 900$  ohm-m<sup>2</sup> above the background modal value of 3000 ohm-m<sup>2</sup>, as expected for the reservoir.

Similar to Myer *et al.* (2012), we have not been able to separate the Gearle and reservoir levels. However, unlike Myer *et al.* (2012) the Bayesian posterior PDF does concentrate models with resistive anomalies at the reservoir depth. This in itself, we think is a noteworthy aspect of our result.

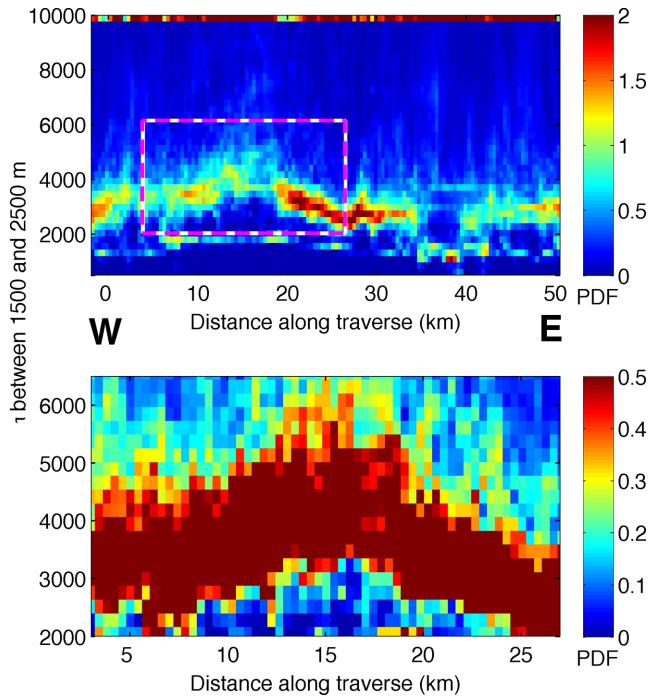


**Figure 13.** Top panel: Probability of integrated resistivity thickness product  $\tau$  between 1500 and 2500-m depth for the Scarborough data inversion. Hotter colours are more probable. The reservoir is seen at roughly 900 ohm-m<sup>2</sup> above the background between 6 and 24 km along the line (dashed box). Throughout the line, the basement  $\tau$  consistently shows up as being the most probable in this depth window. Bottom panel: Same as top, but zoomed in to the reservoir area.

#### 4.4 Comparison with MARE2DEM deterministic 2-D inversion

An inversion over Line 2 utilizing the full range of Rx–Tx offsets ( $\sim 5.5$  km) using the deterministic MARE2DEM code (Key & Ovall 2011; Key 2012) is shown in Fig. 14. This inversion uses 2-D forward model physics and fits the data to rms 1.0. For comparison with the 2-D Bayesian inversion, the MARE2DEM inversion result is shown intersected by two probability cube slices at 11 and 50 km along Line 2 (Fig. 15). The resulting intersections are shown in thick black as profiles along the two slice planes. The most dominant feature from the MARE2DEM inversion at 11 km along the line is high basement resistivity below 2500-m depth. Interestingly, the Bayesian inversion probability slice at 11 km along the line also shows a large change in resistivity PDF near this depth. Both the

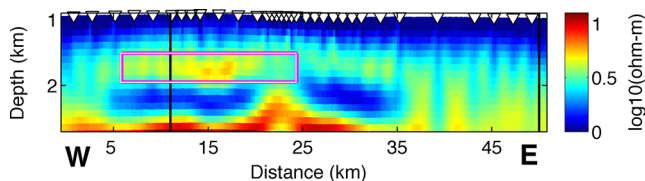


**Figure 14.** The MARE2DEM deterministic inversion result using 2.5-D forward modelling for Scarborough CSEM data over Line 2. Seafloor receivers are shown as white inverted triangles. The most prominent feature is high basement resistivity below 2.5-km depth. The reservoir section (boxed) at  $\sim 1.9$ -km depth is more resistive than its surroundings. Resistivity at 1.9-km depth falls off to lower values towards the east. For purposes of comparison with the probabilistic inversion, two locations for vertical slices have been shown in black at 11 and 50 km. These are the same sections shown in Fig. 11 middle and bottom.

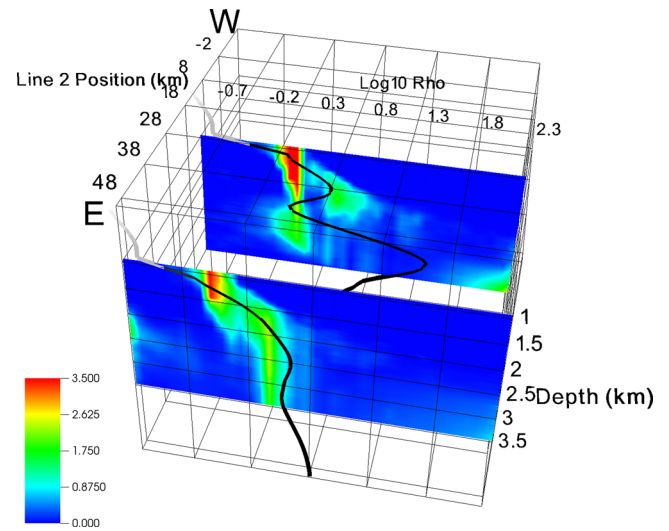


**Figure 15.** Two slices through the Scarborough inversion probability cube shown at 11 km (on reservoir) and 50 km (off reservoir area) along the line, comparing the Bayesian inversion PDFs (proportional to colour hotness) and the MARE2DEM inversion result (thick black line intersecting the two slice planes). The 11-km slice runs through the middle of the reservoir whereas the 50-km slice is 25 km to the east of the 50 per cent gas saturation line. These are at the same locations marked in Fig. 14 and show the same slices as Fig. 11 middle and bottom.

Bayesian posterior PDF and the deterministic inversion show an increase in resistivity at reservoir depth ( $\sim 1950$  m) in this slice. In the slice at 50 km along Line 2, both the deterministic and Bayesian inversions show a much reduced resistivity at reservoir depth, and both are unable to localize the basement resistivity.

The MARE2DEM inversion shows a single model that is more resistive than the background in the reservoir area. Depending on the model regularization philosophy and choices of regularization parameter used, a different result may have been obtained. Furthermore, a single model does not yield any information on the uncertainty with which the model is associated. The Bayesian ensembles do indeed show how the posterior PDFs of resistivity vary in the Earth. However, the Bayesian inversion, though it is parametrized in 2-D, uses a 1-D forward modelling engine and thus approximates the true physics. Both of these results taken jointly, reinforce each other to make a stronger argument for the presence of a reservoir, with an associated uncertainty.

## 5 CONCLUSIONS

We have successfully implemented a flexibly parametrized inversion scheme using 2-D Voronoi cells for CSEM data. In order to accomplish this, we have used a ‘birth/death’ RJ-MCMC algorithm (Green 1995; Bodin & Sambridge 2009; Ray & Key 2012). Synthetic studies were carried out to understand the model space associated with thin, mildly resistive reservoirs. Our results show that the true values of resistivity for these reservoirs are not the most probable, *a posteriori*, and that the integrated resistivity thickness product  $\tau$  is a more robust quantity to examine in these cases. Following the spatial changes in posterior PDFs on both resistivity as well as  $\tau$  yields valuable information on the presence and possible geometries of resistive bodies. Our Bayesian inversion of field data from the Scarborough CSEM survey was successfully able to delineate the reservoir laterally, with a good indication of its depth but not thickness. Comparison with a MARE2DEM deterministic inversion

showed good agreement between the Bayesian and deterministic results with the added benefit of uncertainty about the deterministic result provided by the Bayesian posterior model ensemble. There is a degree of reassurance in the presence of a reservoir provided by the Bayesian posterior model PDF, when *en masse*, unregularized inverted models at certain locations within the Earth tend to be more resistive.

The obvious next step is to move to full 2-D forward modelling of the Voronoi cell models used by our transdimensional algorithm. While 2-D model responses are computationally more expensive than their 1-D counterparts, with the use of accelerated sampling methods such as parallel tempering (Swendsen & Wang 1987; Geyer 1991) in geophysics (Dettmer *et al.* 2011; Dosso *et al.* 2012; Ray *et al.* 2013a; Sambridge 2013) and the advent of highly parallel, cluster-computing oriented 2-D forward codes (Key & Oval 2011), this step is not far away. Finally, we would like to point out that our algorithm is quite flexible and can be applied to various classes of geophysical problems such as surface wave dispersion, seismic receiver functions, etc.

## ACKNOWLEDGEMENTS

We would like to thank the Seafloor Electromagnetic Methods Consortium at the Scripps Institution of Oceanography, UC San Diego for funding this work. TB acknowledges funding support from the Miller Foundation at UC Berkeley. The San Diego Supercomputer Center at UCSD is thanked for providing access to the Triton Shared Computing Cluster. BHP Billiton is thanked for funding the data acquisition project. We would like to thank Jan Dettmer and an anonymous reviewer for their constructive comments.

All 3-D visualizations and probability cube manipulations were carried out using VisIt. The VisIt project is at <http://visit.llnl.gov>.

## REFERENCES

- Abubakar, A., Habashy, T.M., Druskin, V.L., Knizhnerman, L. & Alumbaugh, D., 2008. 2.5D forward and inverse modeling for interpreting low-frequency electromagnetic measurements, *Geophysics*, **73**(4), F165–F177.
- Agostinetti, N.P. & Malinverno, A., 2010. Receiver function inversion by trans-dimensional Monte Carlo sampling, *Geophys. J. Int.*, **181**, 858–872.
- Backus, G.E., 1988. Bayesian inference in geomagnetism, *Geophys. J. Int.*, **92**(1), 125–142.
- Bayes, T. & Price, R., 1763. An essay towards solving a problem in the doctrine of chances. By the Late Rev. Mr. Bayes, F. R. S. Communicated by Mr. Price, in a letter to John Canton, A. M. F. R. S., *Phil. Trans.*, **53**, 370–418.
- Bernardo, J.M. & Smith, A.F.M., 1994. *Bayesian Theory*, Wiley.
- Bodin, T. & Sambridge, M., 2009. Seismic tomography with the reversible jump algorithm, *Geophys. J. Int.*, **178**(3), 1411–1436.
- Bodin, T., Sambridge, M., Tkalčić, H., Arroucau, P., Gallagher, K. & Rawlinson, N., 2012. Transdimensional inversion of receiver functions and surface wave dispersion, *J. geophys. Res.*, **117**(B2), doi:10.1029/2011JB008560.
- Brodie, R.C. & Sambridge, M., 2012. Transdimensional Monte Carlo inversion of AEM Data, in *Proceedings of 22nd International Geophysical Conference and Exhibition*, Brisbane, Australia, no. 1.
- Buland, A. & Kolbjørnsen, O., 2012. Bayesian inversion of CSEM and magnetotelluric data, *Geophysics*, **77**(1), E33–E42.
- Carlin, B.P. & Louis, T.A., 2000. *Bayes and Empirical Bayes Methods for Data Analysis*, CRC Press.
- Chave, A.D. & Cox, C.S., 1982. Controlled electromagnetic sources for measuring electrical conductivity beneath the oceans, 1. Forward problem and model study, *J. geophys. Res.*, **87**(B7), 5327–5338.
- Chen, J., Hoversten, G.M., Vasco, D., Rubin, Y. & Hou, Z., 2007. A Bayesian model for gas saturation estimation using marine seismic AVA and CSEM data, *Geophysics*, **72**(2), WA85–WA95.
- Chen, J., Hoversten, G.M., Key, K., Nordquist, G. & Cumming, W., 2012. Stochastic inversion of magnetotelluric data using a sharp boundary parameterization and application to a geothermal site, *Geophysics*, **77**(4), E265–E279.
- Chib, S. & Greenberg, E., 1995. Understanding the Metropolis-Hastings algorithm, *Am. Stat.*, **49**(4), 327–335.
- Connell, D. & Key, K., 2013. A numerical comparison of time and frequency-domain marine electromagnetic methods for hydrocarbon exploration in shallow water, *Geophys. Prospect.*, **61**, 187–199.
- Constable, S.C., 2006. Marine electromagnetic methods—a new tool for offshore exploration, *Leading Edge*, **25**, 438–444.
- Constable, S., 2010. Ten years of marine CSEM for hydrocarbon exploration, *Geophysics*, **75**(5), 75A67–75A81.
- Constable, S. & Weiss, C.J., 2006. Mapping thin resistors and hydrocarbons with marine EM methods: insights from 1D modeling, *Geophysics*, **71**(2), G43–G51.
- Constable, S.C., Parker, R.L. & Constable, C.G., 1987. Occam's inversion—a practical algorithm for generating smooth models from electromagnetic sounding data, *Geophysics*, **52**(3), 289–300.
- Denison, D.G.T., 2002. *Bayesian Methods for Nonlinear Classification and Regression*, Vol. 386, John Wiley and Sons.
- Dettmer, J. & Dosso, S.E., 2012. Trans-dimensional matched-field geoaoustic inversion with hierarchical error models and interacting Markov chains, *J. acoust. Soc. Am.*, **132**(4), 2239–2250.
- Dettmer, J. & Dosso, S.E., 2013. Probabilistic two-dimensional water-column and seabed inversion with self-adapting parameterizations, *J. acoust. Soc. Am.*, **133**(5), 2612–2623.
- Dettmer, J., Dosso, S.E. & Holland, C.W., 2010. Trans-dimensional geoaoustic inversion, *J. acoust. Soc. Am.*, **128**(6), 3393–3405.
- Dettmer, J., Dosso, S.E. & Holland, C.W., 2011. Sequential trans-dimensional Monte Carlo for range-dependent geoaoustic inversion, *J. acoust. Soc. Am.*, **129**(4), 1794–1806.
- Dettmer, J., Molnar, S., Steininger, G., Dosso, S.E. & Cassidy, J.F., 2012. Trans-dimensional inversion of microtremor array dispersion data with hierarchical autoregressive error models, *Geophys. J. Int.*, **188**(2), 719–734.
- Dosso, S.E., Holland, C.W. & Sambridge, M., 2012. Parallel tempering for strongly nonlinear geoaoustic inversion, *J. acoust. Soc. Am.*, **132**(5), 3030–3040.
- Driscoll, N.W. & Karner, G.D., 1998. Lower crustal extension across the Northern Carnarvon basin, Australia: evidence for an eastward dipping detachment, *J. geophys. Res.*, **103**(B3), 4975–4991.
- Ellingsrud, S., Eidesmo, T., Johansen, S., Sinha, M.C., MacGregor, L.M. & Constable, S., 2002. Remote sensing of hydrocarbon layers by seabed logging (SBL): results from a cruise offshore Angola, *Leading Edge*, **21**, 972–982.
- Gelman, A. & Rubin, D.B., 1992. Inferences from iterative simulations using multiple sequences, *Stat. Sci.*, **7**(4), 457–511.
- Gelman, A., Carlin, J.B., Stern, H.S. & Rubin, D.B., 1995. *Bayesian Data Analysis*, Chapman and Hall/CRC.
- Geyer, C.J., 1991. Markov chain Monte Carlo maximum likelihood, in *Proceedings of the 23rd Symposium on the Interface*, New York, American Statistical Association, p. 156.
- Gilks, W.R., Richardson, S. & Spiegelhalter, D.J., 1996. Introducing Markov chain Monte Carlo, in *Markov Chain Monte Carlo in Practice*, pp. 1–19, Springer.
- Green, P.J., 1995. Reversible jump Markov chain Monte Carlo computation and Bayesian model determination, *Biometrika*, **82**(4), 711–732.
- Gunning, J., Glinsky, M.E. & Hedditich, J., 2010. Resolution and uncertainty in 1D CSEM inversion: a Bayesian approach and open-source implementation, *Geophysics*, **75**(6), F151–F171.
- Hastings, W.K., 1970. Monte Carlo sampling methods using Markov chains and their applications, *Biometrika*, **57**(1), 97–109.
- Hou, Z., Rubin, Y., Hoversten, G.M., Vasco, D. & Chen, J., 2006. Reservoir-parameter identification using minimum relative entropy-based Bayesian

- inversion of seismic AVA and marine CSEM data, *Geophysics*, **71**(6), O77–O88.
- JafarGandomi, A. & Binley, A., 2013. A Bayesian trans-dimensional approach for the fusion of multiple geophysical datasets, *J. appl. Geophys.*, **96**, 38–54.
- Key, K., 2009. 1D inversion of multicomponent, multifrequency marine CSEM data: methodology and synthetic studies for resolving thin resistive layers, *Geophysics*, **74**(2), F9–F20.
- Key, K., 2012. Marine EM inversion using unstructured grids: a 2-D parallel adaptive finite element algorithm, in *SEG Technical Program, Expanded Abstracts*, Las Vegas, no. 9, pp. 1–5.
- Key, K. & Owall, J., 2011. A parallel goal-oriented adaptive finite element method for 2.5-D electromagnetic modelling, *Geophys. J. Int.*, **186**(1), 137–154.
- Liang, F., Liu, C. & Carroll, R., 2011. *Advanced Markov Chain Monte Carlo Methods: Learning from Past Samples*, Vol. 714, Wiley.
- Loseh, L.O., Pedersen, H.M., Ursin, B., Amundsen, L. & Ellingsrud, S., 2006. Low-frequency electromagnetic fields in applied geophysics: waves or diffusion? *Geophysics*, **71**(4), W29–W40.
- Luo, X., 2010. Constraining the shape of a gravity anomalous body using reversible jump Markov chain Monte Carlo, *Geophys. J. Int.*, **180**(3), 1067–1079.
- MacGregor, L. & Sinha, M., 2000. Use of marine controlled-source electromagnetic sounding for sub-basalt exploration, *Geophys. Prospect.*, **48**(6), 1091–1106.
- MacKay, D.J.C., 2003. *Information Theory, Inference and Learning Algorithms*, Cambridge Univ. Press.
- Malinverno, A., 2002. Parsimonious Bayesian Markov chain Monte Carlo inversion in a nonlinear geophysical problem, *Geophys. J. Int.*, **151**(3), 675–688.
- Malinverno, A. & Briggs, V.A., 2004. Expanded uncertainty quantification in inverse problems: hierarchical Bayes and empirical Bayes, *Geophysics*, **69**(4), 1005–1016.
- Minsley, B.J., 2011. A trans-dimensional Bayesian Markov chain Monte Carlo algorithm for model assessment using frequency-domain electromagnetic data, *Geophys. J. Int.*, **187**(1), 252–272.
- Mittet, R. & Gabrielsen, P.T., 2013. Decomposition in upgoing and downgoing fields and inversion of marine CSEM data, *Geophysics*, **78**(1), E1–E17.
- Mittet, R., Brauti, K., Maulana, H. & Wicklund, T.A., 2008. CMP inversion and post-inversion modelling for marine CSEM data, *First Break*, **26**(August), 59–67.
- Mosegaard, K. & Tarantola, A., 1995. Monte Carlo sampling of solutions to inverse problems, *J. geophys. Res.*, **100**(B7), 12 431–12 447.
- Myer, D., Constable, S. & Key, K., 2010. A marine EM survey of the Scarborough gas field, Northwest Shelf of Australia, *First Break*, **28**, 77–82.
- Myer, D., Constable, S. & Key, K., 2011. Broad-band waveforms and robust processing for marine CSEM surveys, *Geophys. J. Int.*, **184**, 689–698.
- Myer, D., Constable, S., Key, K., Glinsky, M.E. & Liu, G., 2012. Marine CSEM of the Scarborough gas field, part 1: experimental design and data uncertainty, *Geophysics*, **77**(4), E281–E299.
- Myer, D., Constable, S. & Key, K., 2013. Magnetotelluric evidence for layered mafic intrusions beneath the Vøring and Exmouth rifted margins, *Phys. Earth planet. Inter.*, **220**, 1–10.
- Neal, R.M., 2003. Slice sampling, *Ann. Stat.*, **31**(3), 705–767.
- Newman, G.A. & Alumbaugh, D.L., 2000. Three-dimensional magnetotelluric inversion using non-linear conjugate gradients, *Geophys. J. Int.*, **140**(2), 410–424.
- Okabe, A., Boots, B., Sugihara, K. & Chiu, S.N., 2009. *Spatial Tessellations: Concepts and Applications of Voronoi Diagrams*, Vol. 501, John Wiley and Sons.
- Ray, A. & Key, K., 2012. Bayesian inversion of marine CSEM data with a trans-dimensional self parametrizing algorithm, *Geophys. J. Int.*, **191**, 1135–1151.
- Ray, A., Alumbaugh, D.L., Hoversten, G.M. & Key, K., 2013a. Robust and accelerated Bayesian inversion of marine controlled-source electromagnetic data using parallel tempering, *Geophysics*, **78**(6), E271–E280.
- Ray, A., Key, K. & Bodin, T., 2013b. Hierarchical Bayesian inversion of marine CSEM data over the Scarborough gas field—a lesson in correlated noise, in *SEG Technical Program Expanded Abstracts*, Houston, pp. 723–727.
- Rosas-Carbajal, M., Linde, N., Kalscheuer, T. & Vrugt, J.A., 2013. Two-dimensional probabilistic inversion of plane-wave electromagnetic data: methodology, model constraints and joint inversion with electrical resistivity data, *Geophys. J. Int.*, **196**(3), 1508–1524.
- Sambridge, M., 2013. A parallel tempering algorithm for probabilistic sampling and multimodal optimization, *Geophys. J. Int.*, **196**(1), 357–374.
- Sambridge, M., Gallagher, K., Jackson, A. & Rickwood, P., 2006. Trans-dimensional inverse problems, model comparison and the evidence, *Geophys. J. Int.*, **167**(2), 528–542.
- Sambridge, M., Bodin, T., Gallagher, K. & Tkalčić, H., 2013. Transdimensional inference in the geosciences, *Phil. Trans. R. Soc. A* (December 2012), **371**(1984), doi:10.1098/rsta.2011.0547.
- Sasaki, Y., 2013. 3D inversion of marine CSEM and MT data: an approach to shallow-water problem, *Geophysics*, **78**(1), E59–E65.
- Scales, J.A. & Sneider, R., 1997. To Bayes or not to Bayes? *Geophysics*, **62**(4), 1045–1046.
- Silva Crepaldi, J.A.L., Pereira Buonora, M.P. & Figueiredo, I., 2011. Fast marine CSEM inversion in the CMP domain using analytical derivatives, *Geophysics*, **76**(5), F303–F313.
- Sisson, S.A., 2005. Transdimensional Markov chains, *J. Am. Stat. Assoc.*, **100**(471), 1077–1089.
- Steininger, G., Dettmer, J., Dosso, S.E. & Holland, C.W., 2013. Trans-dimensional joint inversion of seabed scattering and reflection data, *J. acoust. Soc. Am.*, **133**(3), 1347–1357.
- Swendsen, R.H. & Wang, J.S., 1987. Nonuniversal critical dynamics in Monte Carlo simulations, *Phys. Rev. Lett.*, **58**(2), 86–88.
- Tarantola, A. & Valette, B., 1982. Inverse problems = quest for information, *J. Geophys.*, **50**, 159–170.
- Trainor-Guitton, W. & Hoversten, G.M., 2011. Stochastic inversion for electromagnetic geophysics: practical challenges and improving convergence efficiency, *Geophysics*, **76**(6), F373–F386.
- Vaidyanathan, P.P., Phoong, S.-M. & Lin, Y.-P., 2010. *Signal Processing and Optimization for Transceiver Systems*, Cambridge Univ. Press.
- Veevers, J.J. & Johnstone, M.H., 1974. Comparative stratigraphy and structure of the western Australian margin and the adjacent deep ocean floor, *Initial Rep. DSDP*, **27**, 571–585.
- Voronoi, G., 1908. Nouvelles applications des paramètres continus à la théorie des formes quadratiques. Premier mémoire. Sur quelques propriétés des formes quadratiques positives parfaites, *J. Reine Angew. Math.*, **133**, 97–102.
- Weiss, C., 2007. The fallacy of the ‘shallow-water problem’ in marine CSEM exploration, *Geophysics*, **72**(6), A93–A97.
- Yardim, C. & Gerstoft, P., 2012. Sequential Bayesian techniques applied to non-volcanic tremor, *J. geophys. Res.*, **117**(B10), B10312, doi:10.1029/2012JB009420.
- Young, P.D. & Cox, C.S., 1981. Electromagnetic active source sounding near the East Pacific Rise, *Geophys. Res. Lett.*, **8**, 1043–1046.
- Young, M.K., Rawlinson, N. & Bodin, T., 2013a. Transdimensional inversion of ambient seismic noise for 3D shear velocity structure of the Tasmanian crust, *Geophysics*, **78**(3), WB49–WB62.
- Young, M.K., Tkalčić, H., Bodin, T. & Sambridge, M., 2013b. Global P wave tomography of Earth’s lowermost mantle from partition modeling, *J. geophys. Res.*, **118**(10), 5467–5486.

## APPENDIX A: MATHEMATICAL DETAILS FOR THE TRANSDIMENSIONAL ALGORITHM

### A1 The prior probability

The prior probability density function (PDF) contains information on our knowledge about the subsurface independent of the survey

data. This can be based on data from well-logs, seismic surveys, etc. In the transdimensional formulation, we split the prior into two parts. One part contains information about the number of cells  $k$  in the model,  $p(k)$ . The other part  $p(\mathbf{m}_k|k)$  in our particular case, contains information about the physical parameters associated with a model  $\mathbf{m}_k$  of dimension  $k$ , such as where these cells are, and what the resistivities of these cells are. Using the chain rule, we can thus write

$$p(\mathbf{m}) = p(\mathbf{m}_k, k) = p(\mathbf{m}_k|k) \times p(k), \quad (\text{A1})$$

where

$$\mathbf{m}_k = [\mathbf{z}, \mathbf{x}, \boldsymbol{\rho}], \quad (\text{A2})$$

$$\mathbf{z} = [z_1, z_2, \dots, z_k], \quad (\text{A3})$$

$$\mathbf{x} = [x_1, x_2, \dots, x_k], \quad (\text{A4})$$

$$\boldsymbol{\rho} = [\rho_1, \rho_2, \dots, \rho_k] \quad (\text{A5})$$

and

$$z \in \mathbf{z}, x \in \mathbf{x}, \rho \in \boldsymbol{\rho}. \quad (\text{A6})$$

We use a uniform prior on  $k$ , given by

$$p(k) = \begin{cases} \frac{1}{k_{\max} - k_{\min} + 1} & \text{if } k_{\min} \leq k \leq k_{\max}, \\ 0 & \text{else.} \end{cases} \quad (\text{A7})$$

If we restrict our region of interest to be a rectangle within the vertical plane running through the controlled source electromagnetic (CSEM) survey line, we can define a uniform prior on the position of Voronoi nodes within this rectangle  $p(\mathbf{z}, \mathbf{x})$ . We assume no *a priori* knowledge between the locations of nodes in the model and the Voronoi cell resistivities  $\boldsymbol{\rho}$ . These random variables are independent and therefore their PDFs can be separated in the following product form:

$$p(\mathbf{m}_k|k) = p(\mathbf{z}, \mathbf{x}|k)p(\boldsymbol{\rho}|k). \quad (\text{A8})$$

Voronoi nodes can be located anywhere in the rectangular subsurface area defined by  $[z_{\min}, z_{\max}]$  and  $[x_{\min}, x_{\max}]$ . A given node can be at any of  $K$  (temporarily discrete) points within this rectangle. For  $k$  nodes, we can arrange them without paying attention to their ordering in  $\frac{K!}{k!(K-k)!}$  ways. Note that this unspecified variable  $K$  will cancel out of the expressions we need to use in the algorithm and is only introduced for ease of mathematical derivation. Thus,

$$p(\mathbf{z}, \mathbf{x}|k) = \begin{cases} \left[ \frac{K}{k(K-k)} \right]^{-1} & \text{if } z_{\min} \leq z \leq z_{\max} \text{ and } x_{\min} \leq x \leq x_{\max}, \\ 0 & \text{else.} \end{cases} \quad (\text{A9})$$

An alternative method in prior formulation is to use the Dirichlet prior given in Steininger *et al.* (2013). Assuming that all  $k$  Voronoi cell resistivities within a given model lie uniformly between  $\rho_{\min}$  and  $\rho_{\max}$ , independent of each other, we write

$$p(\boldsymbol{\rho}|k) = \begin{cases} \left[ \frac{1}{\rho_{\max} - \rho_{\min}} \right]^k & \text{if } \rho_{\min} \leq \rho \leq \rho_{\max}, \\ 0 & \text{else.} \end{cases} \quad (\text{A10})$$

To obtain the explicit expression for the prior model probability, we write  $\Delta\rho = \rho_{\max} - \rho_{\min}$  and  $\Delta k = k_{\max} - k_{\min} + 1$  and substitute eqs (A7)–(A10) into (A1) to get

$$p(\mathbf{m}) = \begin{cases} \frac{k!(K-k)!}{K! \Delta k (\Delta\rho)^k} & \text{if } z \in [z_{\min}, z_{\max}], x \in [x_{\min}, x_{\max}], \\ & \rho \in [\rho_{\min}, \rho_{\max}], \forall k \in [k_{\min}, k_{\max}], \\ 0 & \text{else.} \end{cases} \quad (\text{A11})$$

We must mention here that it is natural in geophysical EM to parametrize models using  $\log_{10}(\text{resistivity})$  instead of linear resistivity (e.g. Ray & Key 2012), a practice we have followed in our implementation.

## A2 MH algorithms and the acceptance probability

What guides an Markov chain Monte Carlo (MCMC) sampler like the Metropolis-Hastings (MH) algorithm to convergence upon the posterior PDF is the acceptance probability  $\alpha$  (e.g. Liang *et al.* 2011). At every step of the Markov chain, a candidate model is sampled by perturbing the current model from a known PDF (the proposal PDF  $q$ ) and the acceptance  $\alpha$  is calculated. A random number  $r$  is then sampled uniformly from the interval  $[0,1]$ . If  $r < \alpha$ , the proposed perturbation is accepted, else the old model is retained. The rationale behind this algorithm can be explained by examining in more detail the expression for  $\alpha$  (Bodin & Sambridge 2009), where

$$\alpha(\mathbf{m}'|\mathbf{m}) = \min \left[ 1, \frac{p(\mathbf{m}')}{p(\mathbf{m})} \times \frac{p(\mathbf{d}|\mathbf{m}')}{p(\mathbf{d}|\mathbf{m})} \times \frac{q(\mathbf{m}|\mathbf{m}')}{q(\mathbf{m}'|\mathbf{m})} \times |\mathbf{J}| \right]. \quad (\text{A12})$$

Here,  $\mathbf{m}'$  is the new proposed model and  $\mathbf{m}$  is the old model (throughout this paper, primes will denote new model values). Specifically,  $\frac{p(\mathbf{m}')}{p(\mathbf{m})}$  is the prior ratio,  $\frac{p(\mathbf{d}|\mathbf{m}')}{p(\mathbf{d}|\mathbf{m})}$  is the likelihood ratio and  $\frac{q(\mathbf{m}|\mathbf{m}')}{q(\mathbf{m}'|\mathbf{m})}$  is the proposal ratio. The Jacobian term  $|\mathbf{J}|$  is not to be confused with the model Jacobian needed for gradient-based inversions (e.g. Constable *et al.* 1987), but is a matrix that incorporates changes in model dimension when moving from  $\mathbf{m}$  to  $\mathbf{m}'$ . In a classic MH algorithm with a fixed number of dimensions, the prior ratio (for uniform priors), proposal ratio (for symmetric proposals) and Jacobian term are all 1 (Dettmer *et al.* 2010). Hence, the algorithm always moves towards areas of higher posterior probability if the data misfit improves (likelihood ratio  $> 1$ ). However, it can also move to areas of lower posterior probability with a probability  $\alpha$  if the misfit does not improve (likelihood ratio  $< 1$ ).

To be able to compare likelihoods between models with different numbers of parameters (i.e. with different dimensions), the Jacobian in the acceptance term in eq. (A12) needs to be evaluated. There are various implementations of reversible-jump MCMC (RJ-MCMC), and in all the examples cited so far, a ‘birth–death’ scheme has been used. As shown in Bodin & Sambridge (2009) and Dettmer *et al.* (2010) for the ‘birth–death’ RJ-MCMC scheme, this Jacobian term is unity. We have adopted the ‘birth–death’ algorithm in this paper and shall not concern ourselves with this Jacobian term any further.

As to why the algorithm should not always look to improve the data fit by simply increasing the number of parameters (Voronoi cells in the seabed), if we examine eq. (A12) we find that even if the likelihood ratio times the proposal ratio is greater than one for a proposed move that inserts a new cell into the model, the prior ratio will be less than one owing to the fact that the new prior PDF  $p(\mathbf{m}')$  needs to integrate over a larger number of parameters to equal 1. Hence, there is an opposition to the ‘birth’ of a new layer (which may lead to improvement of data fit) by the prior ratio.

### A3 Outline of our algorithm

We start the algorithm with a very simple model, with  $k = k_{\min}$ . We then allow the algorithm to iteratively add Voronoi nodes ('birth') or remove them ('death'), perturbing the Voronoi cell resistivities, as the data may demand via the acceptance probability  $\alpha$  in (A12). In brief, this is how we proceed:

#### A3.1 Initialization

Start the algorithm with  $k = k_{\min}$  and all resistivities set to that of a uniform 1 ohm-m half-space. The Voronoi nodes are randomly distributed within the prior bounds rectangle.

#### A3.2 Choose one of four moves

(1) Update: Perturb a randomly chosen Voronoi cell resistivity about its current value using a Gaussian proposal  $q(\mathbf{m}'|\mathbf{m})$  with a standard deviation  $\Sigma_{\rho}$ , where

$$q(\mathbf{m}'|\mathbf{m}) = \frac{1}{\sqrt{2\pi}\Sigma_{\rho}} \exp\left[-\frac{1}{2\Sigma_{\rho}^2}(\rho' - \rho)^2\right]. \quad (\text{A13})$$

Note that this update move does not involve a change in the number of cells.

(2) Birth of a new node:  $k' = k + 1$ . In the rectangular area defined by  $[z_{\min}, z_{\max}]$  and  $[x_{\min}, x_{\max}]$ , randomly and with uniform probability we select an unoccupied point and insert a node. This node forms the nucleus for a new Voronoi cell, the resistivity of which is assigned by perturbing the old resistivity value at that location according to a Gaussian proposal with standard deviation  $\Sigma_{bd}$ .

(3) Death of an interface:  $k' = k - 1$ . An existing node is selected at random and deleted.

(4) Move a node location: An existing node is selected at random and its position is perturbed by two independent 1-D Gaussian proposals with standard deviation  $\Sigma_{mz}$  and  $\Sigma_{mx}$  for the  $z$  and  $x$ -directions, respectively. Note that this step does not involve a change in the number of cells either.

At each step, one of these moves is chosen with a certain probability, such that the move probabilities sum to unity. In addition, the birth and death probabilities must be set equal. We set the probabilities as follows:

$$[\text{update, birth, death, move}] \equiv \left[\frac{1}{4}, \frac{1}{4}, \frac{1}{4}, \frac{1}{4}\right].$$

At each step of the Markov chain, the proposed model is evaluated for acceptance. If it is accepted, it becomes the current model. If it is rejected, the current model is preserved and the algorithm moves on to the next step. In order to compute the acceptance, one needs to evaluate eq. (A12), for which we explicitly describe the proposal PDFs and their ratios in the next section.

### A4 Proposal PDFs and acceptance probabilities

#### A4.1 Fixed dimension moves

For all moves that are neither birth nor death, the number of cells remain fixed. In these moves, we have elected to use Gaussian proposals to suggest the new model parameters by centring the proposals on the old parameters and drawing a random number from a normal PDF with a given standard deviation (step size). We can see from eq. (A13) these kinds of moves are symmetric,

implying that the probability to go from the old state to the new state is the same as it would be in going from the new state to the old state:

$$\left[\frac{q(\mathbf{m}|\mathbf{m}')}{q(\mathbf{m}'|\mathbf{m})}\right]_{\text{fixed}} = 1. \quad (\text{A14})$$

Since the number of dimensions remains constant, the prior ratio in eq. (A12) is 1. Hence, for fixed dimension moves, we find that the acceptance probability is simply the ratio of the likelihoods:

$$\alpha_f = \begin{cases} \min\left[1, \frac{\rho(\mathbf{d}|\mathbf{m}')}{\rho(\mathbf{d}|\mathbf{m})}\right] & \text{if } z \in [z_{\min}, z_{\max}], x \in [x_{\min}, x_{\max}], \\ & \rho \in [\rho_{\min}, \rho_{\max}], \\ 0 & \text{else.} \end{cases} \quad (\text{A15})$$

#### A4.2 Birth move

For a birth move, one can select from out of  $K - k$  unoccupied spaces. The perturbation for the birthed cell's resistivity is drawn from a Gaussian with standard deviation  $\Sigma_{bd}$ , centred about the old value in the cell. Since the selection of a position and the perturbations are independent, we can write

$$q(\mathbf{m}'|\mathbf{m}) = q(\mathbf{z}', \mathbf{x}'|\mathbf{m})q(\rho'|\mathbf{m}) \quad (\text{A16})$$

$$= \frac{1}{(K - k)} \frac{1}{\sqrt{2\pi}\Sigma_{bd}} \exp\left[-\frac{(\rho' - \rho)^2}{2\Sigma_{bd}^2}\right]. \quad (\text{A17})$$

For the reverse move in a birth, keeping in mind that the current state has  $k$  cells, there were  $k + 1$  cells to delete from, and the probability of removing resistivities in a cell in the reverse move is 1. Thus, we have

$$q(\mathbf{m}|\mathbf{m}') = q(\mathbf{z}, \mathbf{x}|\mathbf{m}')q(\rho|\mathbf{m}') \quad (\text{A18})$$

$$= \frac{1}{(k + 1)} \times 1. \quad (\text{A19})$$

It follows in a birth move, from eqs (A17) and (A19), that the proposal ratio can be written as

$$\left[\frac{q(\mathbf{m}|\mathbf{m}')}{q(\mathbf{m}'|\mathbf{m})}\right]_{\text{birth}} = \frac{(K - k)\sqrt{2\pi}\Sigma_{bd}}{k + 1} \exp\left[\frac{(\rho' - \rho)^2}{2\Sigma_{bd}^2}\right]. \quad (\text{A20})$$

Finally from eqs (A11), (A12) and (A20) we get for the birth moves, the following acceptance probability:

$$\alpha_b = \begin{cases} \min\left[1, \frac{\sqrt{2\pi}\Sigma_{bd}}{\Delta\rho} \exp\left[\frac{(\rho' - \rho)^2}{2\Sigma_{bd}^2}\right] \frac{\rho(\mathbf{d}|\mathbf{m}')}{\rho(\mathbf{d}|\mathbf{m})}\right] & \rho \in [\rho_{\min}, \rho_{\max}], \\ & \forall k \in [k_{\min}, k_{\max}], \\ 0 & \text{else.} \end{cases} \quad (\text{A21})$$

#### A4.3 Death move

In a death move, one can select one of  $k$  places for deletion. Furthermore, the probability of removing resistivities in a cell is certain. Thus,

$$q(\mathbf{m}'|\mathbf{m}) = q(\mathbf{z}', \mathbf{x}'|\mathbf{m})q(\rho'|\mathbf{m}) \quad (\text{A22})$$

$$= \frac{1}{k} \times 1. \quad (\text{A23})$$

In the reverse move for death, since the reference state has  $k$  interfaces, there are  $K - (k - 1)$  sites at which to add an interface. Furthermore, the resistivity perturbations are proposed using a Gaussian centred around the current value. Hence

$$q(\mathbf{m}|\mathbf{m}') = q(\mathbf{z}, \mathbf{x}|\mathbf{m}')q(\rho|\mathbf{m}') \quad (\text{A24})$$

$$= \frac{1}{K - k + 1} \times \frac{1}{\sqrt{2\pi} \Sigma_{bd}} \exp \left[ -\frac{(\rho - \rho')^2}{2\Sigma_{bd}^2} \right]. \quad (\text{A25})$$

Thus, we can see from eqs (A23) and (A25) that the proposal ratio for death can be written as

$$\left[ \frac{q(\mathbf{m}|\mathbf{m}')}{q(\mathbf{m}'|\mathbf{m})} \right]_{\text{death}} = \frac{k}{(K - k + 1)\sqrt{2\pi} \Sigma_{bd}} \exp \left[ -\frac{(\rho - \rho')^2}{2\Sigma_{bd}^2} \right]. \quad (\text{A26})$$

Again from eqs (A11), (A12) and (A26) we get for the death moves, the following acceptance probability:

$$\alpha_d = \begin{cases} \min \left[ 1, \frac{\Delta\rho}{\sqrt{2\pi} \Sigma_{bd}} \exp \left[ -\frac{(\rho' - \rho)^2}{2\Sigma_{bd}^2} \right] \frac{p(\mathbf{d}|\mathbf{m}')}{p(\mathbf{d}|\mathbf{m})} \right] & \forall k \in [k_{\min}, k_{\max}], \\ 0 & \text{else.} \end{cases} \quad (\text{A27})$$

It should be noted that the derived expressions for  $\alpha$  in eqs (A15), (A21) and (A27) do not involve the variable  $K$  (as promised) and are identical in form to the expressions derived in Bodin & Sambridge (2009).

Furthermore, we mention here that in practice, the log of the acceptance probabilities are calculated and compared against the log of a uniform random number between 0+ and 1. Taking log avoids many problems of numerical stability in the evaluation of eq. (A12).

### A5 Synergy between birth and death

At this juncture, we point out that the birth and death moves operate ‘in concert’. Examining eqs (A21) and (A27), we see that for the same change in the likelihood ratio, the birth and death acceptance probabilities are inverses of each other. The birth move encourages large steps to be taken in the model space, while the death move encourages very small steps in the model space. Thus birth ensures that there should be an increase in dimension, only when the current model is quite different from the proposed model (within the prior bounds, of course). On the other hand, the death move ensures that when the proposed model is very similar to the current one, there should be a decrease in dimensions and an unnecessary cell is then removed.

This synergy between birth and death also explains why the RJ-MCMC algorithm does not keep adding or deleting cells in order to explain the observed data. This is another aspect of Bayesian natural parsimony.

### A6 Convergence to the posterior PDF

The algorithm is run for a given number of steps until it is deemed to have collected enough samples to provide a reasonable estimate of the posterior model PDF. There are a couple of caveats in this regard, as there are with any MCMC sampler (Liang *et al.* 2011). If the algorithm is seeded with an initial model that is in a low posterior probability region, it may take quite a few steps till it reaches a region

of high posterior probability, such that it begins to sample models, most of which fit the data within the given data error. The number of such required steps (which are subsequently discarded in the final chain) is known in MCMC parlance as the ‘burn-in’ period, which depends on how well the proposal PDFs have been scaled (Chib & Greenberg 1995). This brings us to the step sizes (scaling) in the proposal PDFs in the form of the standard deviations  $\Sigma_\rho$ ,  $\Sigma_{mz}$ ,  $\Sigma_{mx}$  and  $\Sigma_{bd}$  required in the various proposals to generate a new candidate model. The form of the proposal PDFs should ‘emulate’ the posterior for efficient sampling, but since the posterior PDF may be complicated (and unknown *a priori*), any kind of simple PDF, symmetric where possible, can be used. The exact form of the proposal does not affect the final solution, at least in theory. For the Scarborough problem, post burn-in we used the following step sizes with Gaussian proposals:

$$[\Sigma_\rho, \Sigma_{mz}, \Sigma_{mx}, \Sigma_{bd}] \equiv [0.1, 10, 150, 0.6],$$

with the resistivity step sizes  $\Sigma_\rho$  and  $\Sigma_{bd}$  specified in  $\log_{10}$  units and the move node step sizes  $\Sigma_{mz}$  and  $\Sigma_{mx}$  in metres.

The suitability of the step size for the problem at hand can be examined by looking at the number of samples accepted in a large interval of steps, referred to as the acceptance rate. If the acceptance rate is too low, it means that the step sizes are too large as lots of steps are falling outside the prior bounds or are being rejected as they land in low-probability (high misfit) areas. If the acceptance rate is too high, then it implies that the algorithm is not exploring the model space enough and will again be slow to converge upon the posterior PDF.

While the sampled posterior should not depend on the size of the steps taken, one has to factor in the optimality of the step size as otherwise convergence will be very slow. For an illuminating discussion on this matter, one can refer to Chib & Greenberg (1995) or Trainor-Guitton & Hoversten (2011) for a more recent discussion relevant to marine CSEM. For further discussions on convergence diagnostics such as Potential Scale Reduction Factors (Gelman & Rubin 1992) and the practicality of their application, one can refer to Liang *et al.* (2011). When the number of parameters is changing, as in RJ-MCMC, it is very challenging to assess convergence and this is still an active area of research (Bodin & Sambridge 2009). A heuristic method to examine speed of convergence is to monitor the ‘distance’ travelled from one sampling step to the next over a window of a certain number of steps. We can project model resistivity values on to an underlying grid, and then look at the norm of the difference between grid values for two successive models. We can then find the average distance travelled over a given step size window.

The algorithm should be run long enough at the lowest acceptable range of rms values (achieved after the burn-in period) such that there is at least stationarity achieved in the square misfit with iteration number. Furthermore, to ensure that the inferred posterior is not biased due to being trapped in local maxima (of the posterior probability), we recommend that the algorithm be run from many different starting points, ideally in parallel for computational efficiency. The final ensemble for posterior inference can be constructed by concatenating the various parallel chains (e.g. Dettmer *et al.* 2010; Bodin *et al.* 2012; Ray & Key 2012). Another means of efficient convergence to the posterior PDF can be to use parallel interacting Markov chains as described in Dettmer & Dosso (2012) and Ray *et al.* (2013a).